LANGMUIR

pubs.acs.org/Langmuir Article

Water Film Structure and Wettability of Different Quartz Surfaces: Hydrogen Bonding Across Various Cutting Planes

Kazuya Kobayashi* and Abbas Firoozabadi*

Cite This: https://doi.org/10.1021/acs.langmuir.3c03165 Read Online

ACCESS | Metrics & More | Article Recommendations | Supporting Information

ABSTRACT: Quartz is ubiquitous in subsurface formations. The crystal faces have different atomic arrangements. Knowledge of the molecular structures on the surface of quartz is key in many processes. Molecular dynamics simulations are conducted to investigate the atomic arrangement effect on the water film structure, ion adsorption, and wettability at three different α-quartz surfaces. The interfacial structures depend on the quartz surface. Intrasurface hydrogen bonding between surface silanols differs in the α-quartz surface. At the (0001) surface, the OH density is 9.58 nm^{-2}, consisting of Q^2 units with two hydroxyl groups per silicone atom. At the $(10\bar{1}0)$-β surface, the OH density is 7.54 nm^{-2}, consisting of Q^3 units with one hydroxyl group per silicone atom; there is significant intrasurface hydrogen bonding. At the $(10\bar{1}0)$-α surface, the OH density is 7.54 nm^{-2}, consisting of Q^2 units; however, there is little intrasurface hydrogen bonding. The intrasurface hydrogen bonding results in the exposure of hydrogen-bond acceptors to the aqueous phase, causing water molecules to have an *H-up* (hydrogen toward surface) orientation. This orientation can be found at the (0001) and $(10\bar{1}0)$-β surfaces; it is related to the degree of ordering at the surface. The ordering at the (0001) and $(10\bar{1}0)$-β surfaces is higher than that at the $(10\bar{1}0)$-α surface. In aqueous systems with ions, cation adsorption is the most dominant at the (0001) surface due to the largest surface density of the intrasurface hydrogen bonding, providing interaction sites for cations to be adsorbed. We observe a pronounced decrease in water film thickness from the ions at the (0001) surface only, likely due to significant cation adsorption. In this work, we demonstrate that the hydrogen-bond network, which varies from the plane cut, affects the water film structure and ion adsorption. The contact is nearly zero despite the changes in the film thickness and molecular structure at the temperature of 318 K.

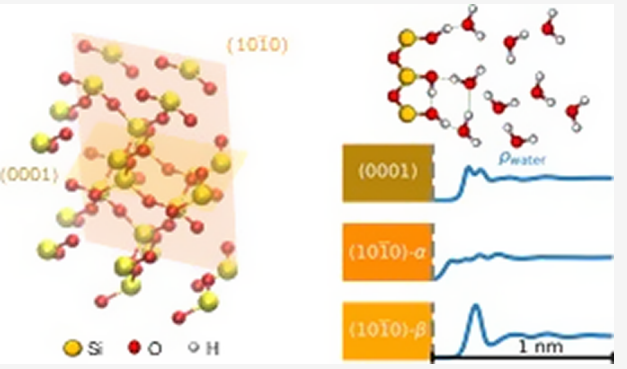

INTRODUCTION

Understanding of the wettability of aqueous surfaces and interfacial structures is critical in various scientific and industrial fields.[1−4] Many physical and chemical processes are influenced by the aqueous interface including colloidal stability, coating, heat transfer, tribology, and flows in porous media. Wettability plays an important role in the efficiency of geological carbon dioxide (CO_2) storage and oil production.[5−7] CO_2 and oil in porous media in subsurface formations are trapped and stabilized by wetting phenomena, known as residual trapping. The capillary entry pressure of caprocks stabilizes the CO_2 plume against the buoyancy force (structural trapping).

Quartz, a crystal form of silica, is a ubiquitous mineral in subsurface formations and may influence various interfacial processes.[8] Wettability and interfacial structures have been extensively investigated for quartz/silica surfaces. The contact angle at the quartz/silica surface, a quantitative measure of wettability, has been reported by numerous authors.[9−16] Contact angles vary from strongly water-wet to intermediate-wet under certain conditions.[16] Contact angle measurements pose various challenges: errors are associated with experimental procedures (pre-equilibration time and length-scale of measurements), surface roughness, and contamination. In quartz/water systems, contact angles vary from zero with pretreatment by piranha solution or plasma to a range of 13.5°−63.5° with pretreatment in petroleum ether, acetone, ethanol, and water.[16]

The contact angle (θ) is described by Young's equation:

$$\cos\theta = \frac{\gamma_{sg} - \gamma_{sw}}{\gamma_{gw}} \quad (1)$$

where γ represents interfacial tensions, and subscripts sg, sw, and gw represent the interfaces between solid and gas, solid and water, and gas and water, respectively. At the nanoscale, θ may diverge from the prediction of eq 1 due to the water film adjacent

Received: October 18, 2023
Revised: February 2, 2024
Accepted: February 2, 2024

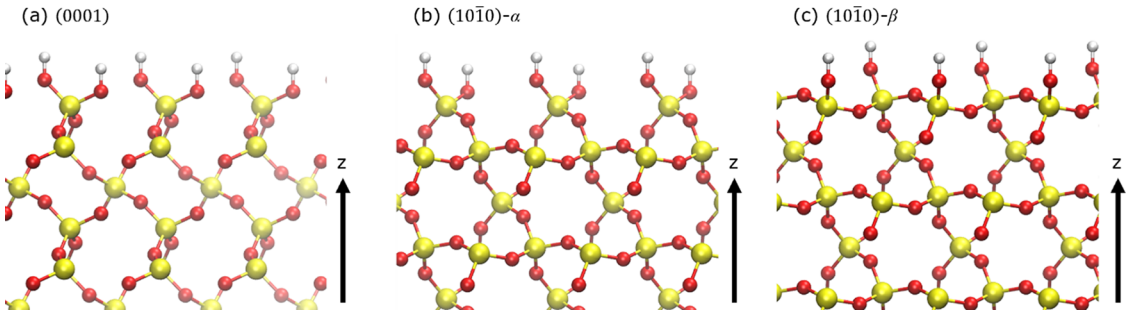

Figure 1. Structure of three types of α-quartz surfaces (side view): (a) (0001), (b) (10$\bar{1}$0)-α, and (c) (10$\bar{1}$0)-β. The (0001) and (10$\bar{1}$0)-α surfaces consist of Q^2 units, while the (10$\bar{1}$0)-β surface consists of Q^3 units. Red, yellow, and white particles represent oxygen, silicon, and hydrogen atoms, respectively.

to the droplet[17] and the line tension[18] when the curvature is high. The water film may significantly influence wetting dynamics[3] at the nanoscale and fluid trapping in porous media.

The structure of the aqueous interface on quartz/silica has been investigated using atomic force microscopy,[19,20] X-ray reflectivity,[20] and sum-frequency vibrational spectroscopy.[21−27] A charge may develop from the deprotonation/protonation of surface hydroxyl groups.[28] The charge results in specific hydrogen-bond networks at the surface. Despite extensive work in the literature, the interfacial structure has not yet been fully resolved. The *H-up* (hydrogen toward surface) orientation of water is found at high pH (pH of 12) facilitated by hydrogen bonding between water and deprotonated hydroxyl groups at the surface.[22] Even at a low pH (pH of 2), the presence of deprotonated hydroxyl sites is also suggested, as indicated by the observed *H-up* orientation.[22] Myalitsin et al. argue that the deprotonated hydroxyl group is not necessary for water to exhibit the *H-up* orientation.[24] Instead, they propose that hydrogen bonding between the surface silanol groups serves as a hydrogen-bond acceptor for the *H-up* orientation.[24] The discrepancy in their microscopic interpretation is partly attributed to experiments conducted on crystal or amorphous silica.[21−27]

The quartz crystal has no perfect crystallographic cleavage plane.[20,29,30] Different planes lead to variations in the surface density of terminations, specifically hydroxyl groups, which differ on the selected plane. Figure 1 shows the atomistic images of different cutting surfaces of α-quartz. An ideal (0001) surface has an OH density of 9.58 nm^{-2}, while the ideal (10$\bar{1}$0)-α and (10$\bar{1}$0)-β surfaces have an OH density of 7.54 nm^{-2}. The distinction between (10$\bar{1}$0)-α and (10$\bar{1}$0)-β surfaces arises from the termination of silicon atoms (Q number). Q^n units represent nSi−O bonds, resulting in $(4-n)$ hydroxyl groups per unit. The (0001), (10$\bar{1}$0)-α, and (10$\bar{1}$0)-β surfaces have Q^2, Q^2, and Q^3 units, respectively.

The cutting plane and different terminations affect the interfacial properties. Schlegel et al.[20] have investigated the (10$\bar{1}$0) surface of α-quartz equilibrated with distilled water. They demonstrate that the (10$\bar{1}$0) surface consists of 67% β-surface and 33% α-surface, suggesting that the β-surface is more stable than the α-surface.[20] Skelton et al.[31] pointed out that the intrasurface hydrogen bonding (hydrogen bonding between OH of silanol groups at the surface) influences surface hydration. Intrasurface hydrogen bonding is higher at the (10$\bar{1}$0)-β surface than at the (10$\bar{1}$0)-α surface.[31] The authors have found that the number of hydrogen bonds to bridging Si−O−Si oxygens is higher at the α-surface than in the β-surface.[31] This process may result in resistance to the dissolution of the β-surface.

Sum frequency vibrational spectroscopy has been conducted on the (0001) α-quartz surface[19−21] and amorphous silica.[24,27] The (10$\bar{1}$0) surface is investigated by atomic force microscopy.[19] X-ray reflectivity measurements are performed on the (10$\bar{1}$0) and the (10$\bar{1}$1) surfaces.[20] Wettability measurements for quartz are often conducted without reporting surface information. Variations in wettability measurements under the same conditions are likely related to the choice of surfaces. Only a few studies have been conducted to compare the properties of different surfaces.[15,16]

Molecular simulations are performed to understand the interfacial structures of α-quartz on different surfaces. The water structure may differ at the bonded interfacial layer, diffuse layer, and bulk region. The relationship between the signal of sum frequency vibrational spectroscopy and the interfacial structure has been investigated through ab initio and classical molecular dynamics simulations.[32−34] Ab initio calculations reveal a network of hydrogen bonding at the surfaces of quartz and silica.[34−42] Cimas et al. demonstrate that a neutral silanol can induce *H-up* and *H-down* orientations by serving as a hydrogen-bond acceptor and donor, respectively.[42] Molecular simulations are also employed to investigate the wettability and water film structure at the nanoscale.[7,15,16,43−47] Tsuji et al.[43] investigate the wettability of the quartz, water, and CO_2 system at different pressures by molecular dynamics simulations. The pressure dependency of wettability on quartz surfaces aligns with the experimental data.[43] Recently, the wettability of different α-quartz surfaces is investigated by molecular simulations and contact angle measurements, revealing that the surfaces are completely water-wet.[15,16] However, the influence of ions on the wettability of different surfaces has not yet been investigated. Musso et al. demonstrate that different quartz surfaces have different surface−adsorbate (NH_3) energy,[39] and this difference in adsorption can result in distinct wettability states and water film structures. The in-depth study of the effect of ions on the molecular structure and wetting on different quartz surfaces remains very limited.

The main motivation of our study is to systematically investigate interfacial structures, ion adsorptions, and wettabilities of different α-quartz surfaces. We aim to explore the differences in the hydrogen-bond network at the surfaces, wettability, and adjacent water films. Three surfaces of α-quartz are selected for investigation: (0001), (10$\bar{1}$0)-α, and (10$\bar{1}$0)-β surfaces. The pair of (0001) and (10$\bar{1}$0)-α surfaces has a different surface density of hydroxyl groups but it has the same termination (Q^2). The (10$\bar{1}$0)-α and the (10$\bar{1}$0)-β surfaces have the same hydroxyl group surface density but a different termination (Q^2 and Q^3). The effect of ions (NaCl) on various

https://doi.org/10.1021/acs.langmuir.3c03165
Langmuir XXXX, XXX, XXX−XXX

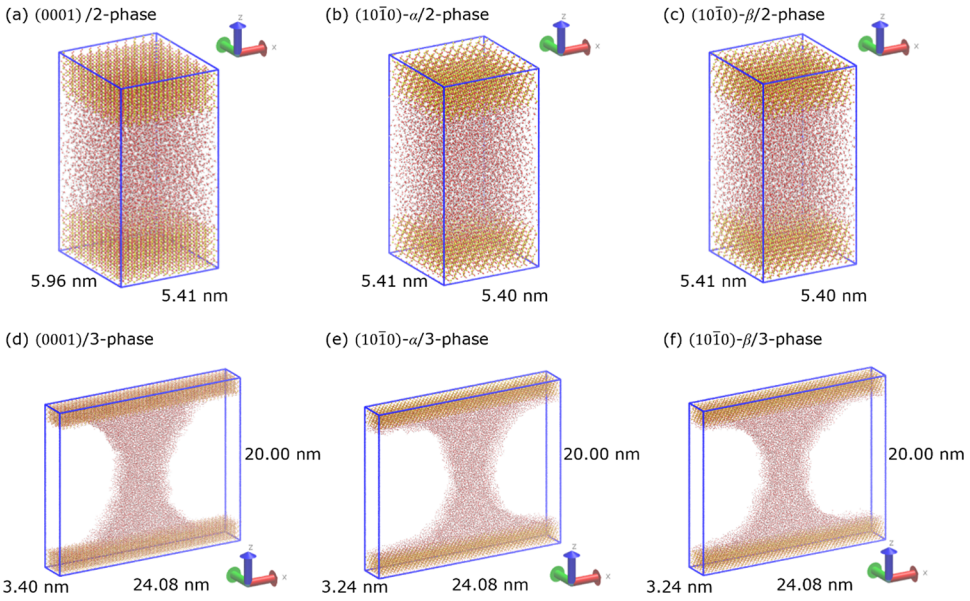

Figure 2. Snapshots of various systems for pure water and brine in two- and three-phase systems. Brine systems have the same size as pure water systems. Two-phase system of: (a) (0001) surface, (b) (10$\bar{1}$0)-α surface, (c) (10$\bar{1}$0)-β surface; three-phase systems of (d) (0001) surface, (e) (10$\bar{1}$0)-α surface, and (f) (10$\bar{1}$0)-β surface. Red, green, and blue arrows represent the x, y, and z axes, respectively. Lengths in the two- and three-phase systems have different scales.

α-quartz surfaces is also investigated; electrolytes may influence both the interfacial structure and wettability.

METHODS

GROMACS 2023.1[48] is used in our molecular dynamics simulations. The CLAYFF[49] and SPC/E[50] force fields are chosen for the mineral and water, respectively. This combination of models is reported to reproduce the structure of the aqueous interface from α-quartz and water.[31] The force field for ions is described by the Joung and Cheatham model,[51] which is compatible with the SPC/E model. Cutoff lengths for Lennard−Jones interactions and Coulombic interactions are set to 1.2 nm with the analytical tail correction[52] and particle mesh Ewald summation[53] applied for treating long-range interactions, respectively. This choice of cutoff length aligns with a previous study using the same force fields.[7] The bond length of water molecules is kept fixed by the LINCS[54] algorithm. We perform calculations for both a two-phase system (liquid and mineral) and a three-phase system (liquid, vapor, and mineral). The thickness of the mineral is greater than 4 nm for all calculations. The sizes of simulation boxes and snapshots of the systems are provided in Figure 2. Periodic boundary conditions are applied in our work. In the systems, there are two interfaces, but we present results for only one interface as consistent results are found for both. We use α-quartz as the mineral, where the unit cell is based on X-ray diffraction by Kihara.[55] The (0001), (10$\bar{1}$0)-α, and (10$\bar{1}$0)-β surfaces are investigated in this study. The surfaces are fully hydroxylated. The two-phase system is employed to investigate fundamental characteristics among different planes. The three-phase system is used to examine the water film structure adjacent to the droplet and wettability. The two-phase system contains 6000 water molecules. The three-phase system consists of 15,000 water molecules. The effect of ions is investigated for 0.95 mol/kg NaCl solutions. We used 108 pairs of NaCl molecules in the two-phase system and 270 pairs of NaCl molecules in the three-phase system. In the three-phase system, the droplet has a cylindrical shape (two-dimensional shape) to eliminate the effect of line tension on the contact angle. Initial configurations of the systems are prepared by combining the liquid phase and solid phase, which are independently equilibrated. The cubic liquid phase and vacuum phase are initially contained in the three-phase system. The liquid changes its shape to represent the wetting on the surface as the system equilibrates. The structure of α-quartz is assumed to be fully flexible. The system is relaxed for 25 ns, followed by a 100 ns production run. The simulation time for the water film to reach equilibrium is reported to be about 10 ns.[7] The two-phase systems are run in the NpT ensemble, and the three-phase systems are run in the NVT ensemble (to allow the formation of two fluid phases). A temperature of 318 K and a pressure of 0.1 MPa are used in the NpT ensemble. The same temperature is used in the NVT ensemble. Both the temperature and pressure are stochastically controlled. Pressure is fixed by changing the box size normal to the surfaces while keeping the surface area constant. Standard deviations (σ) are determined by dividing the 100 ns trajectory into 10 blocks. We include standard deviations in the corresponding figures and tables unless otherwise stated.

The detailed analysis of the water structure is investigated based on the water orientation normal to the surface. We calculate the probability distribution of water orientation, $p(\theta)$, normalized as follows:

$$\int_0^\pi p(\theta)\sin\theta d\theta = 2 \tag{2}$$

The probability distribution $p(\theta)$ equals 1 by this definition when water molecules are randomly oriented. We utilize two intramolecule vectors: the OH vector and the dipole vector. The definitions of the vector and angle are presented in panels a and b in Figure S1. θ is defined as the angle between the two vectors and the direction normal to the surfaces (θ_{OH} and θ_D).

Hydrogen bonding among water molecules and surface hydroxyl groups is analyzed using a geometrical measure. The distance between a donor and an acceptor (r_{DA}) and the angle among hydrogen atoms, the donor, and the acceptor (α_{HDA}) are used in this measure. A pair of donor and acceptor with r_{DA} less than 0.35 nm and α_{HDA} less than 30° is determined as hydrogen-bonded.

RESULTS AND DISCUSSION

The water densities on different surfaces are presented in Figure 3. The structures exhibit dependency on surface chemistry. The highest density (~2400 kg/m^3) is observed at the (10$\bar{1}$0)-β surface (Figure 3, dotted line, z = 0.24 nm), where this surface has a lower hydroxyl density than the (0001) surface. The highest surface density is followed by three bumps (Figure 3, dotted line, z = 0.46 nm, z = 0.64 nm, and z = 0.87 nm). This strong peak aligns with the molecular simulations by Sun et al.[7]

https://doi.org/10.1021/acs.langmuir.3c03165
Langmuir XXXX, XXX, XXX−XXX

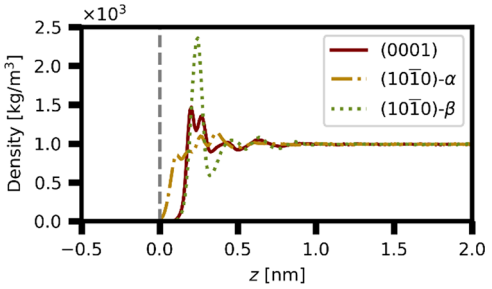

Figure 3. Density distribution of water molecules at the three quartz surfaces. The dashed gray line represents the position of the outermost oxygen atom (hydroxyl oxygen). Error bars are smaller than the line widths.

Two distinct peaks are noticeable near the (0001) surface (Figure 3, solid line, z = 0.20 and z = 0.26 nm), followed by two bumps (Figure 3, solid line, z = 0.43 and z = 0.63 nm). The terminations at the (10$\bar{1}$0) planes, namely, α (Figure 3, dashed dotted line) and β (Figure 3, dotted line), affect water structures. The (10$\bar{1}$0)-α surface consists of Q^2 units, and the (10$\bar{1}$0)-β surface consists of Q^3 units. Water molecules can approach the (10$\bar{1}$0)-α surface more closely than the (10$\bar{1}$0)- β surface; the density of water molecules starts to increase at the position of the outermost hydroxyl groups (the dashed gray line in Figure 3) at the (10$\bar{1}$0)-α surface. The (10$\bar{1}$0)-α surface does not exhibit distinct peaks (Figure 3, dashed dotted line). The hydroxyl density and termination can result in different structures of water at the surfaces.

Water molecules have specific orientations, depending on the distance from the surfaces. Figure 4 illustrates the water orientation at each surface. Red dashed lines represent the peak position in the density distribution from Figure 3. Panels a and b in Figure 4 show the orientation of water molecules at the (0001) surface. θ_{OH} of ∼60° and ∼120° (Figure 4a, z = 0.16 nm) and θ_D of ∼90° (Figure 4b, z = 0.16 nm) represent orientations around the first red dashed line. Another orientation near the red dashed line (Figure 4b, z = 0.21 nm) is characterized by θ_D of ∼180°. Water molecules close to the second red dashed line in panels a and b in Figure 4 have θ_{OH} of ∼170° and θ_D of ∼140°. The orientations result from hydrogen bonding between water molecules and surface hydroxyl groups. Panels a−c in Figure 5 are snapshots of water molecules at the (0001) surface. Hydrogen bonds are indicated by green dotted lines in the snapshots. In Figure 5a, the water molecule has θ_{OH} of 55.9° and 130.6° and θ_D of 94.5°, corresponding to orientations around the first red dashed line. This orientation is the result of two hydrogen bonds: H_{OH} to O_{water} and H_{water} to O_{OH}. Figure 5b

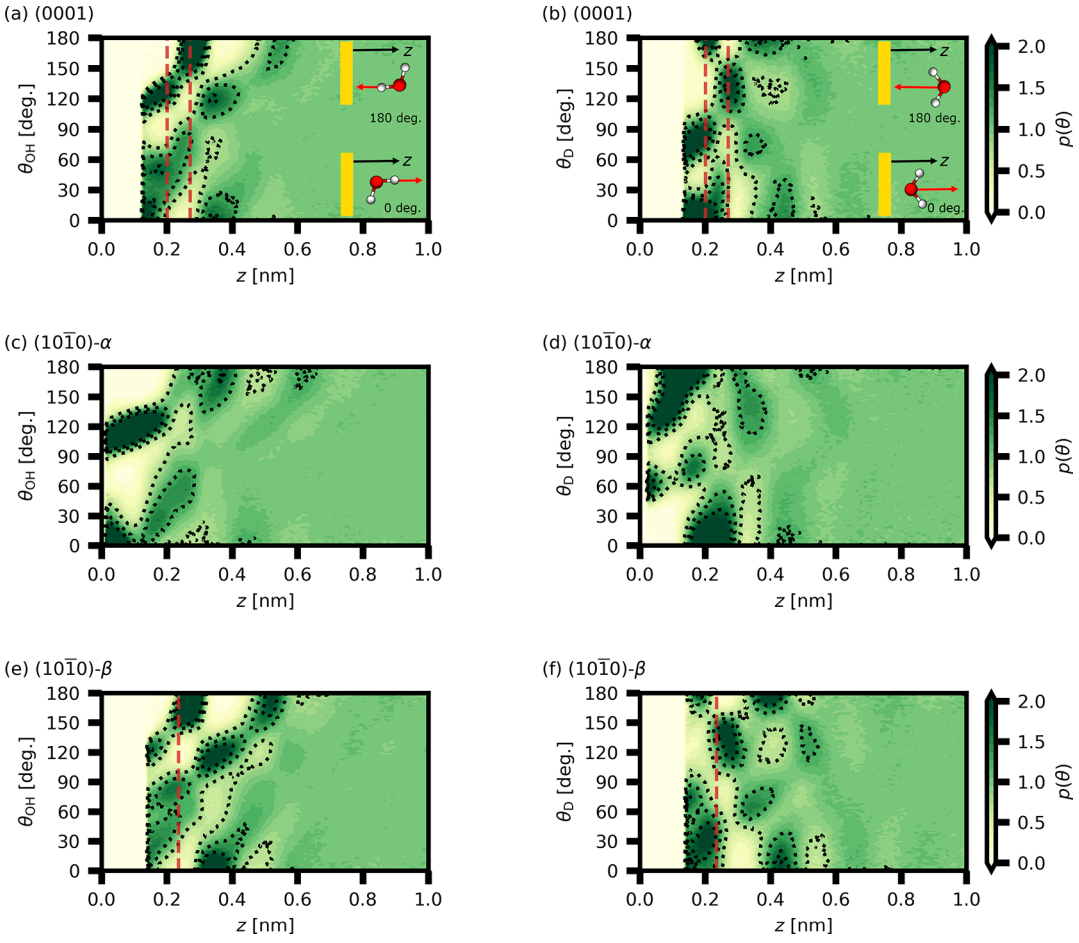

Figure 4. Orientation of water molecules represented by angles between intramolecule vectors (OH vector and dipole vector) and the direction normal to the surface: (a) OH vector at (0001), (b) dipole vector at (0001), (c) OH vector at (10$\bar{1}$0)-α, (d) dipole vector at (10$\bar{1}$0)-α, (e) OH vector at (10$\bar{1}$0)-β, and (f) dipole vector at (10$\bar{1}$0)-β surfaces. z represents the coordinate of the oxygen atom of the water molecule, and z = 0 is the position of the outermost oxygen atoms (hydroxyl oxygen). The red dashed line represents the peak position in the density distributions in Figure 3. The (10$\bar{1}$0)-α surface does not show a distinct peak in water density.

https://doi.org/10.1021/acs.langmuir.3c03165
Langmuir XXXX, XXX, XXX−XXX

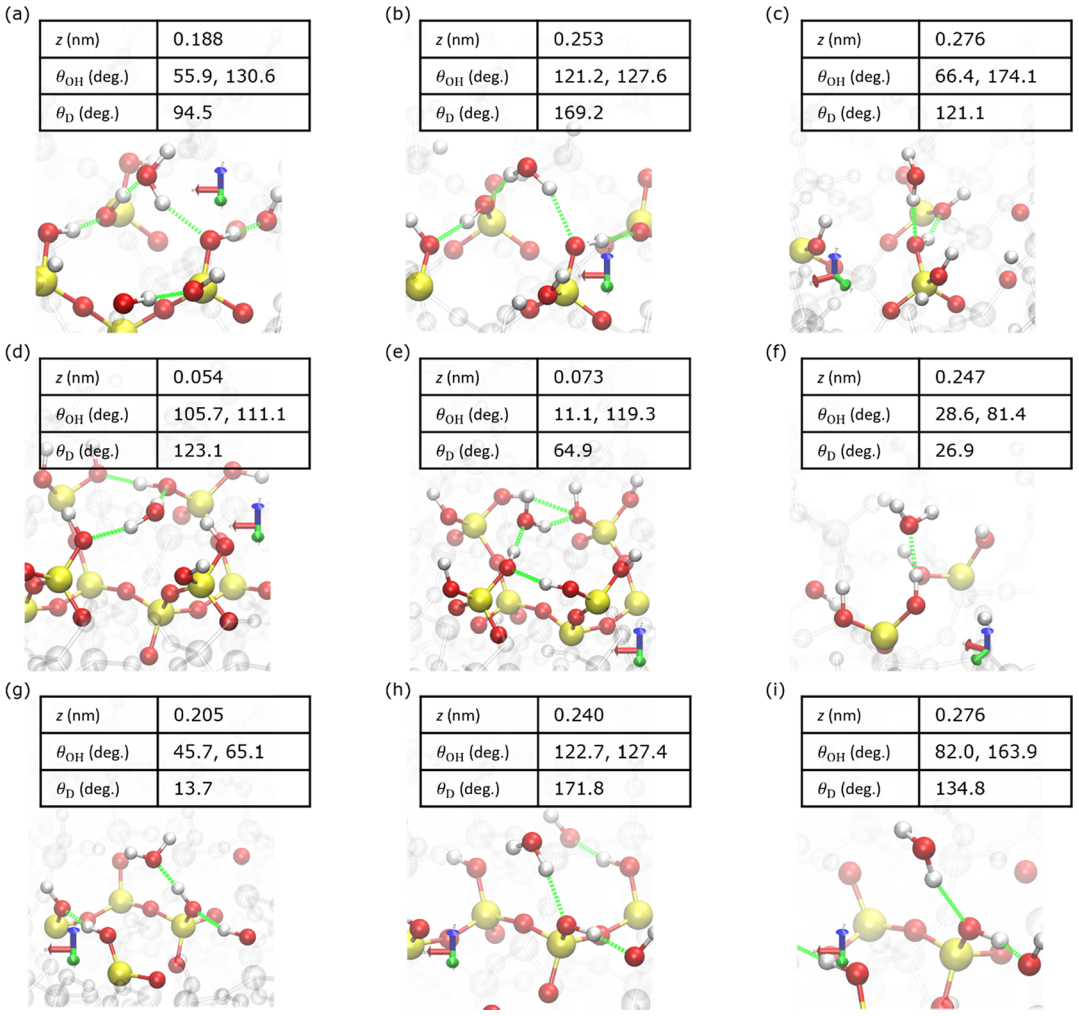

Figure 5. Snapshots of water molecules at the interface in the surfaces of (a–c) (0001), (d–f) $(10\bar{1}0)$-α, and (g–i) $(10\bar{1}0)$-β. z represents the coordinate of the oxygen atom of water molecules. $z = 0$ is the position of the outermost oxygen atoms (hydroxyl oxygen). θ_{OH} and θ_D represent the angle between the intramolecule vector (OH vector and dipole vector) and the direction normal to the surface, respectively. The snapshots can be compared to Figure 4. Green dotted lines show hydrogen bonds. Red, yellow, and white particles represent oxygen, silicon, and hydrogen atoms, respectively. Red, green, and blue arrows represent the x, y, and z axes, respectively.

shows a water molecule with the other orientation at the first red dashed line in panels a and b in Figure 4. This water molecule has θ_{OH} of 121.2° and 127.6° and θ_D of 169.2°, resulting from two H_{water}–O_{OH} hydrogen bonds. In Figure 5c, the water molecule has θ_{OH} of 64.4° and 174.1° and θ_D of 121.1°, representing the orientations around the second red dashed line in panels a and b in Figure 4. The hydrogen bonding between H_{water} and O_{OH} results in the orientation of the water molecule.

Water orientation at the $(10\bar{1}0)$-α surface is shown in panels c and d in Figure 4, with snapshots of representative water molecules shown in panels d–f of Figure 5. The nearest water molecules to the surface have θ_{OH} of ~100° and θ_D of ~120°. A representative snapshot is shown in Figure 5d, where the water molecule has θ_{OH} of 105.7° and 111.1° and θ_D of 123.1°. The hydrogen bonding for the water molecules in Figure 5d is like that of a water molecule at the (0001) surface (Figure 5b), indicating that the orientation is due to two H_{water}–O_{OH} hydrogen bonds. The other peaks of θ_{OH} and θ_D found near the surface are around 10° and 60°, respectively. The water molecules in Figure 5e have an orientation with θ_{OH} of 11.1° and 119.3° and θ_D of 64.9°. Hydrogen bonding in panels a and e of Figure 5 is similar, with two hydrogen bonds (H_{OH} to O_{water} and H_{water} to O_{OH}) in the water molecule. A distinct peak can be found for θ_D (θ_D = 0–30) further from the surface (z = 0.15–0.29 nm) which results from a hydrogen bond between H_{OH} and O_{water} (Figure 5f).

The $(10\bar{1}0)$-β surface exhibits a pattern similar to the (0001) surface, but the peak θ_D around 90° is weaker than that on the (0001) surface (Figure 4b, z = 0.16 nm; Figure 4f, z = 0.18 nm). Instead, we observe a high intensity of θ_D less than 30° (Figure 4f, z = 0.19 nm). A representative water molecule is shown in Figure 5g, having θ_{OH} of 45.7° and 65.1° and θ_D of 13.7°. Hydrogen bonding exists between H_{OH} and O_{water}, but it is missing between H_{water} and O_{OH} (unlike the water molecule in Figure 5a found at the (0001) surface). This missing hydrogen bonding results in a different orientational pattern on the (0001) and $(10\bar{1}0)$-β surfaces. Another high intensity is found for θ_D close to 180° at z = 0.18 nm. The water molecule with hydrogen bonding between H_{water} and the phosphorus molecule of O_{OH} leads to this high intensity (Figure 5h). The water molecule has θ_{OH} of 122.7° and 127.4° and θ_D of 171.8° (Figure 5h). Water orientation next to the red dashed line has peaks at θ_{OH} of ~160° and θ_D of ~130° (panels e and f in Figure 4, z = 0.27 nm). Figure 5i shows a water molecule corresponding to this orientation,

https://doi.org/10.1021/acs.langmuir.3c03165
Langmuir XXXX, XXX, XXX–XXX

having θ_{OH} of 82.0° and 163.9° and θ_D of 134.8°, revealing hydrogen bonding between H_{water} and O_{OH}.

The structure of water in the vicinity of the surfaces strongly depends on the cutting plane and termination through the hydrogen-bond network. We point out that the distance between neighboring hydroxyl groups and intrasurface hydrogen bonds affects the availability of hydrogen-bond donors and acceptors. Figure 6 shows probability distributions of angles (φ)

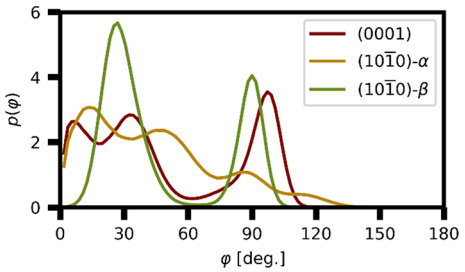

Figure 6. Probability distribution of the angle between hydroxyl groups and the direction normal to various surfaces.

between the OH vector of the hydroxyl groups and the vector normal to the surface. $p(\varphi)$ has the same definition as that represented by eq 2; it will be uniform when hydroxyl groups have a completely random orientation. φ of 90° indicates that hydroxyl groups lie parallel to the surfaces, providing an indication of intrasurface hydrogen bonds. φ of 0° corresponds to hydrogen atoms in the surface hydroxyl groups pointing toward the aqueous phase. The (10$\bar{1}$0)-β and the (0001) surfaces are fully structured; both surfaces have a strong peak around 90°. The peak around 90° results in exposing the hydrogen-bond acceptors to the aqueous phase. A high-intensity area around θ_{OH} of 180° can be found near the (0001) surface and the (10$\bar{1}$0)-β surface but not near the (10$\bar{1}$0)-α surface (panels a, c, and e in Figure 4). This is strongly related to the availability of the hydrogen-bond acceptors from the intrasurface hydrogen bonding. Panels c and i in Figure 5 show the snapshots where intrasurface hydrogen bonds can be observed. Hydroxyl groups lie parallel to the surface to establish hydrogen bonding with another hydroxyl group (shown by green dotted lines in panels c and i in Figure 5). The oxygen atom accepts a hydrogen bond from the water molecule, resulting in θ_{OH} close to 180°. θ_{OH} of 180° is not observed near the (10$\bar{1}$0)-α surface because hydroxyl groups do not lie parallel to the surface. Notably, the (10$\bar{1}$0)-α and (10$\bar{1}$0)-β surfaces have the same OH density (7.54 nm^{-2}). The availability of donors is highly dependent on the formation of intrasurface hydrogen bonds rather than being solely determined by OH density.

The density of hydrogen bonds at the surfaces is summarized in Table 1. Intrasurface hydrogen bonds are significant on the (0001) and (10$\bar{1}$0)-β surfaces, as shown in Figure 6. The density of intrasurface hydrogen bonds for the (0001) surface is higher than that for the (10$\bar{1}$0)-β surface; this results in a higher density of hydrogen-bond acceptors (hydroxyl oxygens). Water molecules for which θ_D is close to 180° have orientations where two hydrogens are toward two hydroxyl oxygens (e.g., panels b and h in Figure 5), namely two hydrogen-bond acceptors from surfaces. The (0001) surface has a higher intensity of this orientation than the (10$\bar{1}$0)-β surface (panels b and f in Figure 4). The higher intensity is probably because of the higher density of intrasurface hydrogen bonds, that is, hydrogen-bond acceptors, for the (0001) surface. The (10$\bar{1}$0)-α surface shows the highest density of intersurface hydrogen bonds.

The *H-up* orientations are found at the (0001) and the (10$\bar{1}$0)-β surfaces (panels a and e in Figure 4, θ_{OH} of 180°). The *H-up* orientation is the result of intrasurface hydrogen bonding. The formation of intrasurface hydrogen bonding is rarely found at the (10$\bar{1}$0)-α surface. The (10$\bar{1}$0)-α surface is less ordered in this context. Pezzotti et al.[34] show that the positive band at 3400 cm^{-1} in SFG spectra is a signature of the crystal-induced ordering of water molecules. The positive band corresponds to water orientation from intrasurface hydrogen bonding. The water molecules shown in panels c and i in Figure 5 are consistent with Pezzotti's rationalizations on the positive band at 3400 cm^{-1}, while the corresponding water orientation cannot be found at the (10$\bar{1}$0)-α surface (Figure 4c).

The variation of structures among the surfaces presented above sheds light on the dominance of the β-surface at the (10$\bar{1}$0) surface rather than at the α-surface. Water molecules can get closer to the (10$\bar{1}$0)-α surface than to the (10$\bar{1}$0)-β surface (Figure 3). Intersurface hydrogen bonding at the (10$\bar{1}$0)-α surface is more significant than that at the (10$\bar{1}$0)-β surface (Table 1). There is a higher probability of water solvating the surface silica units, combined with a difference in the activation energy of silica units for dissolution (Q^2 units, namely α, have lower activation energy than Q^3 units). We point out that intrasurface hydrogen bonds play a critical role in the stability of α-quartz surfaces. There is competition with intersurface hydrogen bonds, as the (0001) surface shows a lower density of intersurface hydrogen bonds (Table 1) and a longer distance of water molecule from the surface (Figure 3). The formation of intrasurface hydrogen bonding from the arrangement of silanol groups is key, rather than the type of silica units at the surfaces. Our simulations agree with the reactive Monte Carlo simulations conducted to investigate the dissolution of β-bristobalite (another type of silica) by Nangia and Garrison.[56]

Table 1. Density of Hydrogen Bonding (n) at Different Surfaces[a]

surface	aqueous phase	n_{intra} (nm^{-2})	n_{inter}^{DW} (nm^{-2})	n_{inter}^{DH} (nm^{-2})
(0001)	pure water	5.634 ± 0.008	4.30 ± 0.02	3.79 ± 0.01
	0.95 mol/kg NaCl sol.	5.544 ± 0.008	3.95 ± 0.03	3.62 ± 0.03
(10$\bar{1}$0)-α	pure water	1.165 ± 0.003	6.339 ± 0.003	5.081 ± 0.003
	0.95 mol/kg NaCl sol.	1.160 ± 0.003	6.17 ± 0.01	4.95 ± 0.01
(10$\bar{1}$0)-β	pure water	3.814 ± 0.002	3.858 ± 0.004	3.551 ± 0.003
	0.95 mol/kg NaCl sol.	3.810 ± 0.001	3.68 ± 0.02	3.415 ± 0.009

[a]Subscript intra represents intrasurface hydrogen bonds (H_{OH} to O_{OH}), subscript inter represents intersurface hydrogen bonds, namely between water and hydroxyl group at the surfaces. Superscripts of DW and DH differentiate the donor of hydrogen bonds: DW (H_{water} to O_{OH}) and DH (H_{OH} to O_{water}).

https://doi.org/10.1021/acs.langmuir.3c03165
Langmuir XXXX, XXX, XXX−XXX

The authors suggest that Q^2 units with intrasurface hydrogen bonds are less reactive than Q^3 units without intrasurface hydrogen bonds.[56] Note that our simulations are not reactive. Reactive modeling will guide the stability of the surfaces. Next, we investigate the effect of salt ions in water on the interface structure and thin film thickness.

Interfacial structures of brines (0.95 mol/kg of NaCl solution) are presented in Figure 7. Ionic structures significantly depend

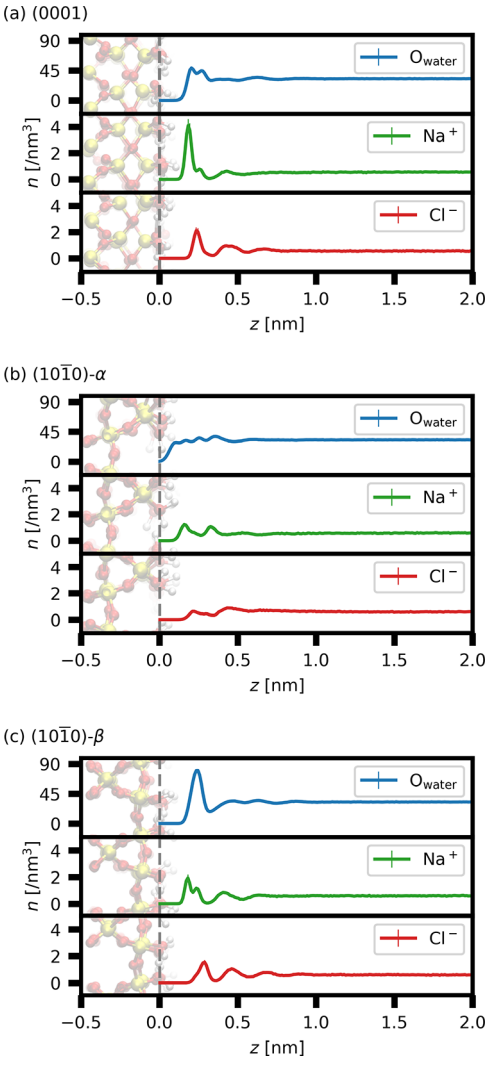

Figure 7. Number density distribution of O_{water} and NaCl ions normal to the surface: (a) (0001), (b) (10$\bar{1}$0)-α, and (c) (10$\bar{1}$0)-β surfaces. The dashed gray line represents the position of the outermost oxygen atoms (hydroxyl oxygen).

on the cutting planes and the termination. Water structures are not affected by the ions, as indicated by the comparison of Figures 3 and 7. The intersurface hydrogen bonds decrease in the presence of ions at the surface (Table 1) due to cation adsorption. The (0001) surface shows strong adsorption of Na^+ cations, followed by a Cl^- peak (Figure 7a). The adsorption of Na^+ cations is lower at the (10$\bar{1}$0)-α and (10$\bar{1}$0)-β surfaces than that at the (0001) surface. The adsorption of water molecules is most pronounced at the (10$\bar{1}$0)-β surface. Snapshots of adsorbed Na^+ cations are shown in Figure S2. Cation adsorption occurs from the surface hydroxyl groups lying parallel to the surface for the cation to interact. The density of intrasurface hydrogen bonding is the most significant at the (0001) surface (Table 1). Adsorbed Na^+ cations are coordinated by two hydroxyl oxygens (Figure S2). The distances between the two hydroxyl oxygens at the (0001), the (10$\bar{1}$0)-α, and the (10$\bar{1}$0)-β surfaces are approximately 0.32, 0.37, and 0.34 nm, respectively. The short distance between the neighboring hydroxyl oxygens, coupled with a high density of intrahydrogen bonds, leads to a high local density of interaction sites; the (0001) surface shows the highest density of Na^+ adsorption.

We evaluated wettability for the three surfaces with pure water and NaCl solution, resulting in six different systems. Contact angles are geometrically determined based on isodensity points, specifically the point of half bulk density for the liquid−vapor interface in geometrical determination. We refer to the position of the outermost oxygen atoms (hydroxyl oxygen) for the definition of the solid surface. The liquid−vapor interface is fitted by a circle excluding the 2 nm region from the surface. The contact angle can be mathematically determined by the interrelation between the fitted circle and the surface (Figure S3). All the systems exhibit completely water-wet, that is, contact angles are zero. This is anticipated because the surfaces are completely hydroxylated. Our simulations align with the experimental and theoretical study of Deng et al.[16] The authors show that different α-quartz surfaces are completely water-wet with pure water.[16] We observe water films adjacent to the droplet. Detailed structural analysis for the adjacent films is conducted by dividing the systems into two slices (Figure 8).

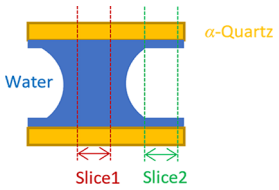

Figure 8. Schematic diagram of the two slices in the three-phase systems. One slice (Slice 1) is inside, and the other slice (Slice 2) is outside the droplet (adsorbed water film).

One slice (Slice 1) is inside the droplet, and the other slice (Slice 2) is outside, representing the adsorbed water film adjacent to the droplet. The shapes of the droplet and the slices are shown in Figure S4. Figure 9 presents a density distribution normal to the surface for the two regions. The water structures (pure water) in Slices 1 and 2 are shown in panels a−e in Figure 9. The first and second peaks are consistent in both slices at the (0001) surface (Figure 9a). The structure of Slice 2 at the (10$\bar{1}$0)-α surface corresponds to Slice 1 up to z = 0.43 nm (Figure 9c). Figure 9e indicates that the adsorbed water film has the same structure up to the first peak at the (10$\bar{1}$0)-β surface.

NaCl ions in water alter the structure of the adsorbed water film at the (0001) surface. Panels b, d, and f in Figure 9 show a comparison of adsorbed water film structures from the NaCl solution. Interfacial structures for the (0001) surface with NaCl solution are shown in Figure 9b. The adsorbed water film (Slice 2) from the NaCl solution is thinner than that from pure water (Figure 9a,b). Table 2 summarizes the thickness of the adsorbed water film defined by the outer position of half of the bulk density. The other surfaces, namely the (10$\bar{1}$0)-α and the (10$\bar{1}$0)-β, show a small decrease in the thickness of the adsorbed water film by NaCl (panels c and f in Figure 9). The decrease is proportional to the amount of the adsorbed cation. Na^+ adsorption is more pronounced on the (0001) surface than on

https://doi.org/10.1021/acs.langmuir.3c03165
Langmuir XXXX, XXX, XXX−XXX

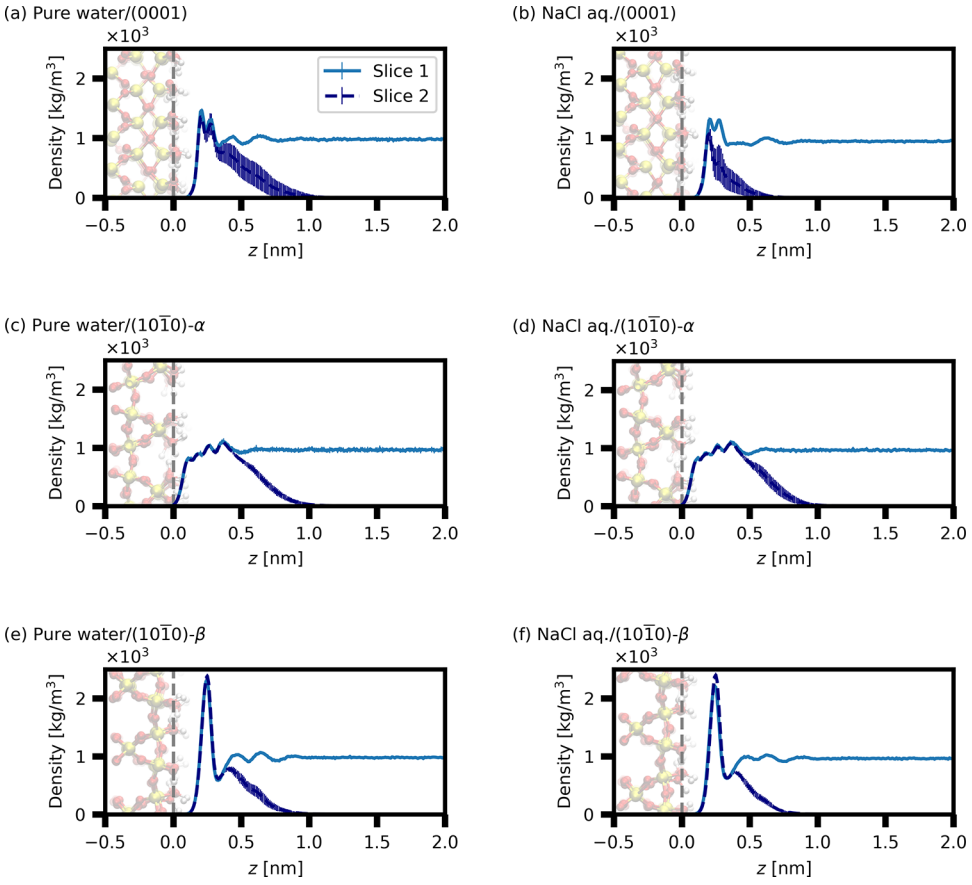

Figure 9. Water film density in the three-phase systems: (a,b) (0001), (c,d) (10$\bar{1}$0)-α, and (e,f) (10$\bar{1}$0)-β surfaces. The left panels (a,c,e) are for pure water, and the right panels (b,d,f) are for brine (0.95 mol/kg NaCl solution). The dashed gray line represents the position of the outermost oxygen atoms (hydroxyl oxygen).

Table 2. Adsorbed Water Film Thickness (nm)

surface	pure water	NaCl aq.	diff.
(0001)	0.5 ± 0.1	0.30 ± 0.07	0.2 ± 0.1
(10$\bar{1}$0)-α	0.66 ± 0.03	0.63 ± 0.04	0.03 ± 0.05
(10$\bar{1}$0)-β	0.55 ± 0.05	0.49 ± 0.02	0.06 ± 0.05

the others (Figures 7 and S5 for Slice 1 in the three-phase systems). The interfacial tension between the aqueous phase and the surface decreases due to adsorption, potentially resulting in a decrease in the water film thickness by the ions.

Interference between the two interfaces, namely, solid−liquid and liquid−vapor, is observed in the adsorbed water film at the (0001) surface when the water film becomes thin. Water orientation of Slice 2 for pure water and NaCl solution is shown in Figure 10. The corresponding plots for the (10$\bar{1}$0)-α and the (10$\bar{1}$0)-β surfaces are presented in Figures S6 and S7, where no significant changes in water orientations are observed. At the (0001) surface, water orientations with θ_D of 180° and 0° decrease by the addition of NaCl (comparing panels b and d in Figure 10). The water orientation at the liquid−vapor interface has a θ_D of 90°. To the best of our knowledge, no measurements of changes in the water orientation under these conditions have been reported. When the adsorbed water film becomes thin, we do not observe two different orientations (θ_D of 0° and 180°). The investigation of changes in water film structures as a function of the water film thickness will be pursued in future studies.

CONCLUSIONS

α-Quartz exhibits a variety of cutting planes with different surface hydroxyl densities and terminations. Molecular dynamics simulations provide insights into the effect of terminations and hydroxyl density on the water film structures. The simulations demonstrate that interfacial structures are significantly influenced by the surface chemistry. Varied molecular structures emerge due to the exposure of the hydrogen-bond acceptors to the aqueous phase resulting from the formation of intrasurface hydrogen bonds on α-quartz surfaces. Notably, the (0001) and the (10$\bar{1}$0)-β surfaces show substantial intrasurface hydrogen bonding, while the (10$\bar{1}$0)-α surface does not. The (10$\bar{1}$0)-α surface displays different water orientations near the surface due to lower intrasurface hydrogen bonding. The *H*-up orientation is observed exclusively at the (0001) surface and (10$\bar{1}$0)-β surface. This orientation indicates a higher degree of ordering for these surfaces compared to the (10$\bar{1}$0)-α surface, attributable to the intrasurface hydrogen bonds. The proximity of hydrogen-bond acceptors to the aqueous phase creates interaction sites for cations to be adsorbed. The adsorbed cations coordinate with two hydroxyl oxygens on all surfaces. Cation adsorption is the most pronounced on the (0001) surface, which has the highest surface density of intrasurface hydrogen bonding. We observe a decrease in the thickness of the adsorbed water film due to pronounced adsorption on the (0001) surface. This decrease is proportional to the adsorbed amount of the cation. In this study, we demonstrate that the hydrogen-bond network varies across different cutting planes,

https://doi.org/10.1021/acs.langmuir.3c03165
Langmuir XXXX, XXX, XXX−XXX

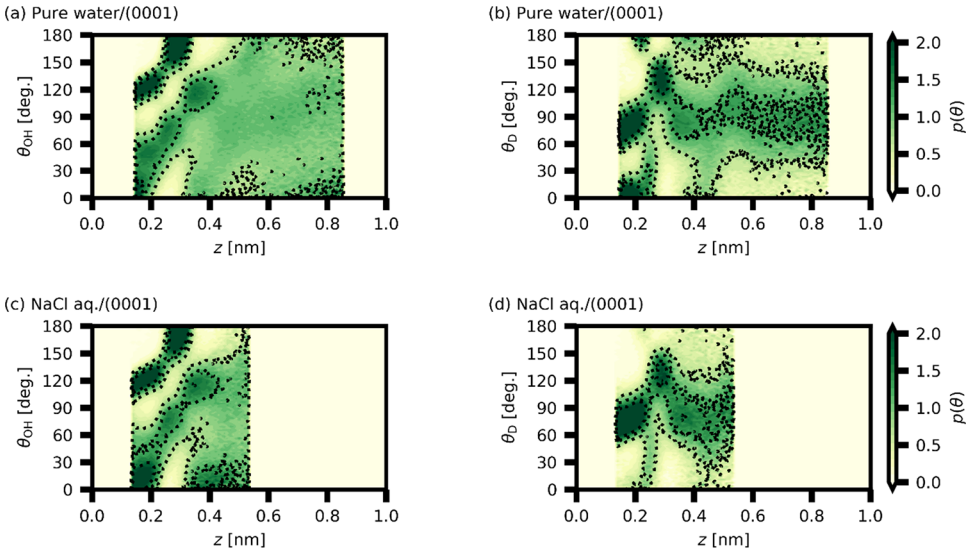

Figure 10. Orientation of water molecules in the adsorbed water film (Slice 2) represented by angles between intramolecule vectors (OH vector and dipole vector) and the direction normal to the (0001) surface: (a) OH vector in the pure water system, (b) dipole vector in the pure water system, (c) OH vector in the NaCl aq. system, and (d) dipole vector in the NaCl aq. system. z represents the z-coordinate of the oxygen atom of the water molecule. $z = 0$ is the position of the outermost oxygen atoms (hydroxyl oxygen).

leading to a significant change in water film structure and ion adsorption. Despite all differences in molecular structures and liquid film thickness, the contact angle is close to zero at a temperature of 318 K. In future studies, one may investigate wetting at higher temperatures.

■ ASSOCIATED CONTENT

Supporting Information

The Supporting Information is available free of charge at https://pubs.acs.org/doi/10.1021/acs.langmuir.3c03165.

Definition of intramolecule vectors and angles; snapshots of adsorbed Na^+; schematic diagram of the geometrical determination of contact angles; density map of water molecule from three-phase systems; number density distribution from three-phase systems; and water orientation of adsorbed water film at the $(10\bar{1}0)$-α and the $(10\bar{1}0)$-β surfaces (PDF)

■ AUTHOR INFORMATION

Corresponding Authors

Kazuya Kobayashi − *INPEX Corporation, Tokyo 107-6332, Japan; Department of Chemical and Biomolecular Engineering, Rice University, Houston, Texas 77005, United States*; Email: kazuya.kobayashi@inpex.co.jp, kazuya.kobayashi@rice.edu

Abbas Firoozabadi − *Department of Chemical and Biomolecular Engineering, Rice University, Houston, Texas 77005, United States*; orcid.org/0000-0001-6102-9534; Email: abbas.firoozabadi@rice.edu

Complete contact information is available at: https://pubs.acs.org/10.1021/acs.langmuir.3c03165

Author Contributions

The manuscript was written through contributions of all authors. All authors have given approval to the final version of the manuscript.

Notes

The authors declare no competing financial interest.

■ ACKNOWLEDGMENTS

The authors would like to thank the member companies of the RERI for their support.

■ REFERENCES

(1) Björneholm, O.; Hansen, M. H.; Hodgson, A.; Liu, L.-M.; Limmer, D. T.; Michaelides, A.; Pedevilla, P.; Rossmeisl, J.; Shen, H.; Tocci, G.; Tyrode, E.; Walz, M.-M.; Werner, J.; Bluhm, H. Water at Interfaces. *Chem. Rev.* **2016**, *116*, 7698−7726.

(2) Extrand, C. W. Origins of Wetting. *Langmuir* **2016**, *32*, 7697−7706.

(3) Wang, H. From Contact Line Structures to Wetting Dynamics. *Langmuir* **2019**, *35*, 10233−10245.

(4) Banuelos, J. L.; Borguet, E.; Brown, G. E.; Cygan, R. T.; DeYoreo, J. J.; Dove, P. M.; Gaigeot, M.-P.; Geiger, F. M.; Gibbs, J. M.; Grassian, V. H.; Ilgen, A. G.; Jun, Y.-S.; Kabengi, N.; Katz, L.; Kubicki, J. D.; Lützenkirchen, J.; Putnis, C. V.; Remsing, R. C.; Rosso, K. M.; Rother, G.; Sulpizi, M.; Villalobos, M.; Zhang, H. Oxide- and Silicate-Water Interfaces and Their Roles in Technology and the Environment. *Chem. Rev.* **2023**, *123*, 6413−6544.

(5) Bourg, I. C.; Beckingham, L. E.; DePaolo, D. J. The Nanoscale Basis of CO2 Trapping for Geologic Storage. *Environ. Sci. Technol.* **2015**, *49*, 10265−10284.

(6) Liang, Y.; Tsuji, S.; Jia, J.; Tsuji, T.; Matsuoka, T. Modeling CO2−Water−Mineral Wettability and Mineralization for Carbon Geo-sequestration. *Acc. Chem. Res.* **2017**, *50*, 1530−1540.

(7) Sun, E. W.-H.; Bourg, I. C. Molecular Dynamics Simulations of Mineral Surface Wettability by Water Versus CO2: Thin Films, Contact Angles, and Capillary Pressure in a Silica Nanopore. *J. Phys. Chem. C* **2020**, *124*, 25382−25395.

(8) Schulz, M. S.; White, A. F. Chemical Weathering in a Tropical Watershed, Luquillo Mountains, Puerto Rico III: Quartz Dissolution Rates. *Geochim. Cosmochim. Acta* **1999**, *63*, 337−350.

(9) Jung, J.-W.; Wan, J. Supercritical CO2 and Ionic Strength Effects on Wettability of Silica Surfaces: Equilibrium Contact Angle Measurements. *Energy Fuels* **2012**, *26*, 6053−6059.

(10) Farokhpoor, R.; Bjørkvik, B. J. A.; Lindeberg, E.; Torsæter, O. Wettability Behavior of CO_2 at Storage Conditions. *Int. J. Greenhouse Gas Control* **2013**, *12*, 18−25.

(11) Wang, S.; Edwards, I. M.; Clarens, A. F. Wettability Phenomena at the CO_2-Brine-Mineral Interface: Implications for Geologic Carbon Sequestration. *Environ. Sci. Technol.* **2013**, *47*, 234−241.

(12) Saraji, S.; Goual, L.; Piri, M.; Plancher, H. Wettability of Supercritical Carbon Dioxide/Water/Quartz Systems: Simultaneous Measurement of Contact Angle and Interfacial Tension at Reservoir Conditions. *Langmuir* **2013**, *29*, 6856−6866.
(13) Bikkina, P. K. Contact Angle Measurements of CO_2-Water-Quartz/Calcite Systems in the Perspective of Carbon Sequestration. *Int. J. Greenhouse Gas Control* **2011**, *5*, 1259−1271.
(14) Arif, M.; Abu-Khamsin, S. A.; Iglauer, S. Wettability of Rock/CO2/Brine and Rock/Oil/CO2-Enriched-Brine Systems: Critical Parametric Analysis and Future Outlook. *Adv. Colloid Interface Sci.* **2019**, *268*, 91−113.
(15) Deng, Y.; Wu, Q.; Li, Z.; Huang, X.; Rao, S.; Liang, Y.; Lu, H. Crystal Face Dependent Wettability of α-Quartz: Elucidation by Time-of-Flight Secondary Ion Mass Spectrometry Techniques Combined with Molecular Dynamics. *J. Colloid Interface Sci.* **2022**, *607*, 1699−1708.
(16) Deng, Y.; Li, Z.; Rao, S.; Zheng, H.; Huang, X.; Liu, Q.; Wang, D.; Lu, H. Mechanism for the Effects of Surface Chemical Composition and Crystal Face on the Wettability of α-Quartz Surface. *Appl. Surf. Sci.* **2023**, *633*, No. 157559.
(17) Mugele, F.; Bera, B.; Cavalli, A.; Siretanu, I.; Maestro, A.; Duits, M.; Cohen-Stuart, M.; van den Ende, D.; Stocker, I.; Collins, I. Ion Adsorption-induced Wetting Transition in Oil-Water-Mineral Systems. *Sci. Rep.* **2015**, *5*, 10519.
(18) Firoozabadi, A. *Thermodynamics and Applications in Hydrocarbon Energy Production*; McGraw-Hill, 2016; Chapter VI.
(19) Nagai, S.; Urata, S.; Suga, K.; Fukama, T.; Hayashi, Y.; Miyazawa, K. Three-Dimensional Ordering of Water Molecules Reflecting Hydroxyl Groups on Sapphire (001) and α-Quartz (100) Surfaces. *Nanoscale* **2023**, *15*, 13262−13271.
(20) Schlegel, M. L.; Nagy, K. L.; Fenter, P.; Sturchio, N. C. Structures of Quartz $(10\bar{1}0)$- and $(10\bar{1}1)$-Water Interfaces Determined by X-ray Reflectivity and Atomic Force Microscopy of Natural Growth Surfaces. *Geochim. Cosmochim. Acta* **2002**, *66*, 3037−3054.
(21) Kim, J.; Kim, G.; Cremer, P. S. Investigation of Water Structure at the Solid/Liquid Interface in the Presence of Supported Lipid Bilayers by Vibrational Sum Frequency Spectroscopy. *Langmuir* **2001**, *17*, 7255−7260.
(22) Ostroverkhov, V.; Waychunas, G. A.; Shen, Y. R. New Information on Water Interfacial Structure Revealed by Phase-Sensitive Surface Spectroscopy. *Phys. Rev. Lett.* **2005**, *94*, No. 046102.
(23) Ohno, P. E.; Saslow, S. A.; Wang, H.; Geiger, F. M.; Eisenthal, K. B. Phase-Referenced Nonlinear Spectroscopy of the α-Quartz/Water Interface. *Nat. Commun.* **2016**, *7*, 13587.
(24) Myalitsin, A.; Urashima, S.; Nihonyanagi, S.; Yamaguchi, S.; Tahara, T. Water Structure at the Buried Silica/Aqueous Interface Studied by Heterodyne-Detected Vibrational Sum-Frequency Generation. *J. Phys. Chem. C* **2016**, *120*, 9357−9363.
(25) Lyu, Y.; Wang, Y.; Wang, S.; Liu, B.; Du, H. Potassium Hydroxide Concentration-Dependent Water Structure on the Quartz Surface Studied by Combining Sum-Frequency Generation (SFG) Spectroscopy and Molecular Simulations. *Langmuir* **2019**, *35*, 11651−11661.
(26) Rehl, B.; Gibbs, J. M. Role of Ions on the Surface-Bound Water Structure at the Silica/Water Interface: Identifying the Spectral Signature of Stability. *J. Phys. Chem. Lett.* **2021**, *12*, 2854−2864.
(27) Wei, F.; Urashima, S.; Nihonyanagi, S.; Tahara, T. Elucidation of the pH-Dependent Electric Double Layer Structure at the Silica/Water Interface Using Heterodyne-Detected Vibrational Sum Frequency Generation Spectroscopy. *J. Am. Chem. Soc.* **2023**, *145*, 8833−8846.
(28) Zhuravlev, L. T. Concentration of Hydroxyl Groups on the Surface of Amorphous Silicas. *Langmuir* **1987**, *3*, 316−318.
(29) Bloss, G. D.; Gibbs, G. V. Cleavage in Quartz. *Am. Mineral.* **1963**, *48*, 821−838.
(30) Goumans, T. P. M.; Wander, A.; Brown, W. A.; Catlow, C. R. A. Structure and Stability of the (001) α-Quartz Surface. *Phys. Chem. Chem. Phys.* **2007**, *9*, 2146−2152.
(31) Skelton, A. A.; Wesolowski, D. J.; Cummings, P. T. Investigating the Quartz $(10\bar{1}0)$/Water Interface Using Classical and Ab Initio Molecular Dynamics. *Langmuir* **2011**, *27*, 8700−8709.
(32) Smirnov, K. S. Structure and Sum-Frequency Generation Spectra of Water on Neutral Hydroxylated Silica Surfaces. *Phys. Chem. Chem. Phys.* **2021**, *23*, 6929−6949.
(33) Smimov, K. S. A Molecular Dynamics Study of the Nonlinear Spectra and Structure of Charged (101) Quartz/Water Interfaces. *Phys. Chem. Chem. Phys.* **2022**, *24*, 25118.
(34) Pezzotti, S.; Galimberti, D. R.; Gaigeot, M.-P. Deconvolution of BIL-SFG and DL-SFG Spectroscopic Signals Reveals Order/Disorder of Water at the Elusive Aqueous Silica Interface. *Phys. Chem. Chem. Phys.* **2019**, *21*, 22188−22202.
(35) Rimola, A.; Costa, D.; Sodupe, M.; Lambert, J.-F.; Ugliengo, P. Silica Surface Features and Their Role in the Adsorption of Biomolecules: Computational Modeling and Experiments. *Chem. Rev.* **2013**, *113*, 4216−4313.
(36) Sulpizi, M.; Gaigeot, M.-P.; Sprik, M. The Silica-Water Interface: How the Silanols Determine the Surface Acidity and Modulate the Water Properties. *J. Chem. Theory Comput.* **2012**, *8*, 1037−1047.
(37) Pfeiffer-Laplaud, M.; Gaigeot, M.-P. Electrolytes at the Hydroxylated (0001) α-Quartz/Water Interface: Location and Structural Effects on Interfacial Silanols by DFT-Based MD. *J. Phys. Chem. C* **2016**, *120*, 14034−14047.
(38) Musso, F.; Mignon, P.; Ugliengo, P.; Sodupe, M. Cooperative Effects at Water-Crystalline Silica Interfaces Strengthen Surface Silanol Hydrogen Bonding. An *ab initio* Molecular Dyamics Study. *Phys. Chem. Chem. Phys.* **2012**, *14*, 10507−10514.
(39) Musso, F.; Ugliengo, P.; Sodupe, M. Do H-Bond Features Silica Surfaces Affect the H_2O and NH_3 Adsorption? Insights from Periodic B3LYP Calculations. *J. Phys. Chem. A* **2011**, *115*, 11221−11228.
(40) Murashov, V. V.; Demchuk, E. A Comparative Study of Unrelaxed Surfaces on Quartz and Kaolinite, Using the Periodic Density Functional Theory. *J. Phys. Chem. B* **2005**, *109*, 10835−10841.
(41) Chen, Y.-W.; Chu, I.-H.; Wang, Y.; Cheng, H.-P. Water Thin Film-Silica Interaction on α-Quartz (0001) Surfaces. *Phys. Rev. B* **2011**, *84*, No. 155444.
(42) Cimas, Á.; Tielens, F.; Sulpizi, M.; Gaigeot, M.-P.; Costa, D. The Amorphous Silica-Liquid Water Interface Studied by *ab initio* Molecular Dynamics (AIMD): Local Organization in Global Disorder. *J. Phys.: Condens. Matter* **2014**, *26*, No. 244106.
(43) Tsuji, S.; Liang, Y.; Kunieda, M.; Takahashi, S.; Matsuoka, T. Molecular Dynamics Simulations of the CO_2-Water-Silica Interfacial Systems. *Energy Procedia* **2013**, *37*, 5435−5442.
(44) Liu, X.; Cheng, J.; Lu, X.; Wang, R. Surface Acidity of Quartz: Understanding the Crystallographic Control. *Phys. Chem. Chem. Phys.* **2014**, *16*, 26909.
(45) Javanbakht, G.; Sedghi, M.; Welch, W.; Goual, L. Molecular Dynamics Simulations of CO2/Water/Quartz Interfacial Properties: Impact of CO2 Dissolution in Water. *Langmuir* **2015**, *31*, 5812−5819.
(46) Jiménez-Ángeles, F.; Firoozabadi, A. Contact Angle, Liquid Film, and Liquid−Liquid and Liquid−Solid Interfaces in Model Oil−Brine−Substrate Systems. *J. Phys. Chem. C* **2016**, *120*, 11910−11917.
(47) Abramov, A.; Keshavarz, A.; Iglauer, S. Wettability of Fully Hydroxylated and Alkylated (001) α-Quartz Surface in Caron Dioxide Atmosphere. *J. Phys. Chem. C* **2019**, *123*, 9027−9040.
(48) Abraham, M.; Alekseenko, A.; Bergh, C.; Blau, C.; Briand, E.; Doijade, M.; Fleischmann, S.; Gapsys, V.; Garg, G.; Gorelov, S.; Gouaillardet, G.; Gray, A.; Irrgang, M. E.; Jalalypour, F.; Jordan, J.; Junghans, C.; Kanduri, P.; Keller, S.; Kutzner, C.; Lemkul, J. A.; Lundborg, M.; Merz, P.; Miletić, V.; Morozov, D.; Páll, S.; Schulz, R.; Shirts, M.; Shvetsov, A.; Soproni, B.; Van Der Spoel, D.; Turner, P.; Uphoff, C.; Villa, A.; Wingbermühle, S.; Zhmurov, A.; Bauer, P.; Hess, B.; Lindahl, E. *GROMACS 2023.1 Manual*; Zenodo, 2023, DOI: 10.5281/zenodo.7852189.
(49) Cygan, R.; Liang, J.-J.; Kalinichev, A. G. Molecular Models of Hydroxide, Oxyhydroxide, and Clay Phases and the Development of a General Force Field. *J. Phys. Chem. B* **2004**, *108*, 1255−1266.
(50) Berendsen, H. J. C.; Gringera, J. R.; Straatsma, T. P. The Missing Term in Effective pair Potentials. *J. Phys. Chem.* **1987**, *91*, 6269−6271.

https://doi.org/10.1021/acs.langmuir.3c03165
Langmuir XXXX, XXX, XXX−XXX

(51) Joung, I. S.; Cheatham, T. E., III Determination of Alkali and Halide Monovalent Ion Parameters for Use in Explicitly Solvated Biomolecular Simulations. *J. Phys. Chem. B* **2008**, *112*, 9020−9041.
(52) Allen, M. P.; Tildesley, D. J. *Computer Simulation of Liquids*, 2nd ed.; Oxford University Press: Oxford, U.K., 2017.
(53) Darden, T.; York, D.; Pedersen, L. Particle Mesh Ewald: An Nlog(N) Method for Ewald Sums in Large Systems. *J. Chem. Phys.* **1993**, *98*, 10089−10092.
(54) Hess, B.; Bekker, H.; Berendsen, H. J. C.; Fraaije, J. G. E. M. LINCS: A Linear Constraint Solver for Molecular Simulations. *J. Comput. Chem.* **1997**, *18*, 1463−1472.
(55) Kihara, K. An X-ray Study of the Temperature Dependence of the Quartz Structure. *Eur. J. Mineral.* **1990**, *2*, 63−78.
(56) Nangia, S.; Garrison, B. J. Role of Intrasurface hydrogen Bonding on Silica Dissolution. *J. Phys. Chem. C* **2010**, *114*, 2267−2272.

https://doi.org/10.1021/acs.langmuir.3c03165
Langmuir XXXX, XXX, XXX−XXX